HAL
open science

Automatic landing on aircraft carrier by visual servoing

L. Coutard, F. Chaumette, J.-M. Pflimlin

To cite this version:

L. Coutard, F. Chaumette, J.-M. Pflimlin. Automatic landing on aircraft carrier by visual servoing. IEEE/RSJ Int. Conf. on Intelligent Robots and Systems, IROS'11, 2011, San Francisco, USA, United States. pp.2843-2848. hal-00639673

HAL Id: hal-00639673

https://inria.hal.science/hal-00639673v1

Submitted on 9 Nov 2011

HAL is a multi-disciplinary open access archive for the deposit and dissemination of scientific research documents, whether they are published or not. The documents may come from teaching and research institutions in France or abroad, or from public or private research centers.

L'archive ouverte pluridisciplinaire **HAL**, est destinée au dépôt et à la diffusion de documents scientifiques de niveau recherche, publiés ou non, émanant des établissements d'enseignement et de recherche français ou étrangers, des laboratoires publics ou privés.

Automatic landing on aircraft carrier by visual servoing

Laurent Coutard, François Chaumette and Jean-Michel Pflimlin

***Abstract*— The landing on carrier is a very difficult task even for trained pilots. This paper presents a method to land automatically using aircraft sensors and three visual features inspired by visual cues used by pilots. These features whose link with the aircraft state is established, are introduced in a control scheme using a linearized aircraft model. The control law demonstrates a large convergence domain using simulated visual features and a 3D tracker applied on synthetic images.**

I. Introduction

Landing on an aircraft carrier is usually considered by pilots as one of the most difficult exercise, complicated by visibility conditions, carrier dynamics and small landing area. In function of visibility conditions, several approaches toward the carrier are used, as presented in [1]. In our case, the studied trajectory consists in beginning the descent at 7.5 km from the carrier and in putting the hook on a desired descent glide. To ensure landing accuracy, no flare is performed. Method can be sum up by keeping the descent rate and angle of attack constant to maintain the aircraft stability and to prevent it from stall.

Control of landing on carrier is not a new problem. It was studied using classical sensors as radar or relative GPS [2], which determine the error wrt a reference trajectory and correct it using a control law that can be optimal [3] or robust [4]. Some prediction model of the carrier dynamics is implemented in [3] to improve the control.

Visual features used during the landing by the pilot were studied for several decades for cognitive and safety aspects. The aim was to understand what features are used by pilots and to determine their sensibility [5] in order to model the human reactions and improve the pilot training. [6] presents a quite complete state of the art of visual features used to control the aircraft during the alignment, the approach and the landing. For example, the distance between the vanishing and the impact points allows pilots to follow the descent glide. The link between relative pose and visual features is established considering low angle assumption in [7] and [8]. The landing on carrier was mainly studied under the scope of aiding systems dealing with the visibility of the optical landing systems. One of the methods used by naval pilots to land on carrier is to control its aircraft in order to focus the glide slope vector present on the Head-Up-Display (HUD) to a triangle mark on the deck as presented in Fig. 1a. Another cue is the angle between the drop line and the deck line that is used by pilots to align wrt the landing deck (see Fig. 1b). This feature provides nice decoupling properties because the segments forming this angle are orthogonal in 3D.

Laurent Coutard and François Chaumette are with INRIA Rennes-Bretagne Atlantique and IRISA, Campus de Beaulieu, 35042 Rennes cedex, France {Laurent.Coutard, Francois.Chaumette}@inria.fr

Jean-Michel Pflimlin is with Dassault Aviation 78, Quai Marcel Dassault - 92552 Saint Cloud Cedex 300 Jean-Michel.Pflimlin@dassault-aviation.com

(a) (b)

Fig. 1. (a) Pilots try to put the HUD velocity vector at the basis of the triangle mark in order to follow the glide slope; (b) The angle between the drop and the alignment lines (yellow and dash) provides lateral information

Visual servoing allows the control of a dynamic system using visual features as inputs. Features can be the estimated pose by vision (3D features) or point coordinates or line angles in the image (2D features). Classical visual servoing is well defined for six DOF robot controlled in velocity [9]. This is not the case of aircrafts, which are non-holonomic and under-actuated systems and are not directly controllable in velocity. Visual servoing was used in previous works to land on static runway [10][11][12]. At the authors knowledge, it was never used for landing on a moving deck.

In order to design a control law, most of the works model the aircraft as linearized in the space state during the approach or alignment phase of landing. The difference between these works relies on the choice of the features and on the kind of controller. [10][13][11] and [14] use as image features the vanishing point and the composition of angles of the projected runway lines. This set of features presents good decoupling properties. [12] uses as visual feature an homography matrix that is the transformation between two images representing the same planar scene. Non linear control scheme using aircraft sensors (Inertial Measurement Unit, Pitot tubes) and camera is studied in [15]. Features are expressed in Plücker coordinates and used to build a centroid vector that is used as input of the control law. In order to improve aircraft behavior, [11] takes into account aircraft dynamics by modifying the desired features along the aircraft trajectory. In order to be robust to the wind, classical proportional integral scheme is applied in [10][14][12] and a wind estimator is built in [15].

This paper presents a new set of three visual features for the landing on aircraft carrier: the x-coordinate of the vanishing point, the distance in the image between the

vanishing and impact points, and the angle between deck axis and its width. The second and third features have never been used before. A classical control scheme based on a linearized aircraft model of the Rafale allows the carrier landing even when it moves. Whereas some desired features used in [11][14][12] are varying along the glide and need some external information to be computed, our desired features remain constant during the task and they are defined in function of the desired glide. Images are provided by the Damocles designation and recognition pod from Thales Optronics [1]. It is located under the aircraft on its right-side and has two fields-of-view (1 and 4°) and has Roll-Tilt degrees of freedom. This imaging sensor is well suited for this application because the detection and tracking has to be effected in wide space [1]. Other sensors embedded on the aircraft can be used as Inertial Measurement Unit (IMU). Moreover, the method is independent of GPS and landing aids systems presented in [1].

The paper is organized as follow: modeling of the aircraft is described in Section II, visual features are investigated in Section III. Using the control law defined in Section IV, simulation results are presented in Section V.

II. Modeling

A. Aircraft model

This section presents the different frames involved, notations and the aircraft dynamics linearized model.

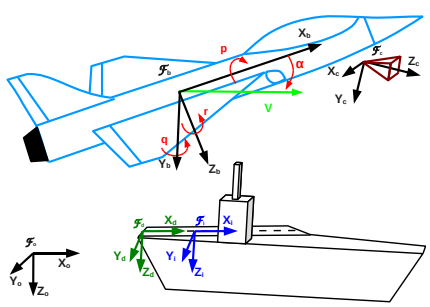

Fig. 2. Frames and velocities

$\mathcal{F}_o$, $\mathcal{F}_b$ and $\mathcal{F}_c$ are respectively a fixed reference, aircraft and camera frames, as presented in Fig. 2. $\mathcal{F}_d$ corresponds to the deck frame, along which the impact frame $\mathcal{F}_i$ is located on the x-axis with the same orientation than $\mathcal{F}_d$. Pitch and roll orientation of the carrier are not taken into account in this study. The pose vector of the aircraft in $\mathcal{F}_i$ is defined by $\mathbf{P} = (\mathbf{p}, \Phi) = (X, Y, Z, \phi, \theta, \psi)$, where the orientation Φ is represented using Euler angles [16]. The aircraft velocity screw in the aircraft frame $\mathcal{F}_b$ is defined by $\mathbf{v}_b = (\upsilon_b, \omega_b) = (u, v, w, p, q, r)$, whose three first and last components are respectively linear and rotational parts. Both velocity screw $\mathbf{v}_b$ and orientation Φ are provided by the Inertial Measurement Unit. V and α are respectively the aerodynamics velocity and the angle of attack and are provided by pitot tubes. Y, Z and ψ can be related to visual information. Assuming flat-earth hypothesis (neglecting the accelerations produced by the Earth rate), some kinematics relations can be derived using the Direct Cosine Matrix $\mathbf{B_B}$ and the attitude propagation matrix ξ [16], respectively defined by:

$$\begin{cases} \dot{\Phi} = \xi(\Phi)\ \omega_b \\ \dot{\mathbf{p}} = \mathbf{B}_B^{\mathrm{T}}\ \upsilon_b \end{cases} \tag{1}$$

Considering classical small ϕ and ψ angles, and low movement assumption, which is respected for the flight phase, the model is linearized at an equilibrium flight configuration:

$$\mathbf{B_B} = \begin{bmatrix} c\theta_0 & 0 & -s\theta_0 \\ 0 & 1 & 0 \\ s\theta_0 & 0 & c\theta_0 \end{bmatrix}; \xi^{-1} = \begin{bmatrix} 1 & 0 & -s\theta_0 \\ 0 & 1 & 0 \\ 0 & 0 & c\theta_0 \end{bmatrix} \tag{2}$$

where θ_0 is the trim value of the aircraft pitch for this flight configuration. $c\theta_0 = \cos\theta_0$ and $s\theta_0 = \sin\theta_0$.

Aircraft dynamics is defined by a non-linear model [16]. A classical method to study a system in order to design a control scheme is to consider a linearization point. For this trim point, longitudinal and lateral motion (respectively defined with $_{lg}$ and $_{lt}$ subscripts) are supposed decoupled:

$$\begin{bmatrix} \dot{\tilde{\mathbf{x}}}_{lg} \\ \dot{\tilde{\mathbf{x}}}_{lt} \end{bmatrix} = \begin{bmatrix} \mathbf{A}_{lg} & \mathbf{0} \\ \mathbf{0} & \mathbf{A}_{lgt} \end{bmatrix} \begin{bmatrix} \tilde{\mathbf{x}}_{lg} \\ \tilde{\mathbf{x}}_{lt} \end{bmatrix} + \begin{bmatrix} \mathbf{B}_{lg} & \mathbf{0} \\ \mathbf{0} & \mathbf{B}_{lgt} \end{bmatrix} \begin{bmatrix} \tilde{\mathbf{u}}_{lg} \\ \tilde{\mathbf{u}}_{lt} \end{bmatrix} \tag{3}$$

where $\tilde{\mathbf{x}}_{lg} = \left(\tilde{V},\ \tilde{\alpha},\ \tilde{\theta},\ \tilde{q},\ \tilde{Z}\right)$ and $\tilde{\mathbf{x}}_{lt} = \left(\tilde{p},\ \tilde{r},\ \tilde{\phi},\ \tilde{\psi},\ \tilde{Y}\right)$. $\tilde{\mathbf{x}}$ and $\tilde{\mathbf{u}}$ express the variations of the state $\mathbf{x}$ and the inputs $\mathbf{u}$ around the linearization point defined by $\mathbf{x}_0$ and $\mathbf{u}_0$ as $\tilde{\mathbf{x}} = \mathbf{x} - \mathbf{x}_0$ and $\tilde{\mathbf{u}} = \mathbf{u} - \mathbf{u}_0$.

As many modern aircrafts, fly-by-wire augmentation stability systems control the aircraft. Thus, longitudinal and lateral control inputs, $\mathbf{u}_{lg}$ and $\mathbf{u}_{lt}$ are respectively the commanded normal acceleration a_{z_c}, the throttle τ and the commanded roll-rate p_c.

B. Camera

The orientation of the camera is fixed in the aircraft frame and is equal to:

$${}^c\mathbf{R}_b = \begin{bmatrix} 0 & 1 & 0 \\ 0 & 0 & 1 \\ 1 & 0 & 0 \end{bmatrix} \begin{bmatrix} c\theta_c & 0 & -s\theta_c \\ 0 & 1 & 0 \\ s\theta_c & 0 & c\theta_c \end{bmatrix} \tag{4}$$

with $\theta_c = -\theta_0 + \delta_0$ is the tilt angle of the camera, where $\delta_0 = -\tan^{-1}\frac{Z_0}{X_0}$ is the glide slope angle to the impact point (δ_0 is about -4°). X_0 and Z_0 are longitudinal and altitude distances in $\mathcal{F}_i$ at the linearization point. This camera orientation allows to implicitly center the impact point of the carrier in the image all along the desired landing trajectory.

III. Visual Features

As presented in Section I, visual features choose as inputs of the control scheme for the autonomous landing, rely on visual cues used by pilots. Proposed visual features $\mathbf{s}$ are represented on Fig. 3. To control the longitudinal motion, the distance l_y is well adapted because it is representative of the angle δ between impact point and horizon line as presented on Fig. 4. l_y corresponds to the distance between the vanishing and the impact points along the y-axis of the image. In order to maintain a constant glide slope, l_y

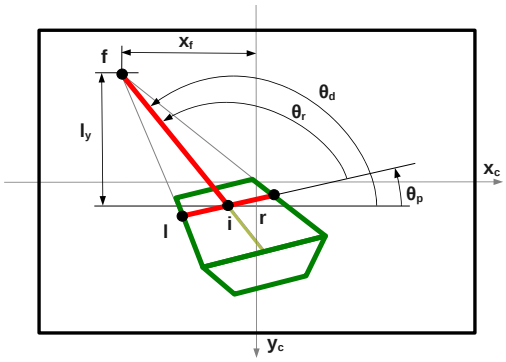

Fig. 3. Features l_y, x_f and θ_r in a general configuration

has to be regulated to a constant desired value which is approximately equal to the desired glide angle.

In order to align to the deck, the x-axis position of the vanishing point x_f (commonly used in [10][13][11]) and the angle θ_r are used. The angle θ_r is defined by two orthogonal segments belonging to the deck plane. Both provide information related to the cap and lateral position between carrier and aircraft. For example, configuration of Fig. 3 lets think that the camera is placed at the left of the deck alignment line and is not oriented in the deck axis.

At the authors knowledge, we recall that features l_y and θ_r were never used before in visual servoing to land on static or moving runway, while we will see they allow obtaining satisfactory results.

A. Visual features modeling

The relation between the camera velocity $\mathbf{v}_c$ (expressed in the camera frame $\mathcal{F}_c$) and visual features $\mathbf{s}$ is defined by the interaction matrix $\mathbf{L_s}$ [9]:

$$\dot{\mathbf{s}} = \mathbf{L_s}\ \mathbf{v}_c \tag{5}$$

with the well-known form for an image point:

$$\mathbf{L_x} = \begin{bmatrix} \mathbf{L}_x \\ \mathbf{L}_y \end{bmatrix} = \begin{bmatrix} \frac{-1}{Z} & 0 & \frac{x}{Z} & xy & -(1+x^2) & y \\ 0 & \frac{-1}{Z} & \frac{y}{Z} & 1+y^2 & -xy & -x \end{bmatrix} \tag{6}$$

where x, y, Z are respectively the x and y coordinates of the point in the image and the depth of the 3D point in the camera frame. The interaction matrix of the vanishing point corresponds to equation (6) considering Z tends to infinity, leading to invariance wrt any translational motion.

In the general case, the interaction matrix of a segment orientation $\theta = \tan^{-1}(\frac{y_1-y_2}{x_1-x_2})$ (using coordinates of points $\mathbf{x}_1$ and $\mathbf{x}_2$) is defined by:

$$\mathbf{L}_\theta = \begin{bmatrix} \frac{D}{l}\ s\theta \\ \frac{-D}{l}\ c\theta \\ -D(x_m\ s\theta - y_m\ c\theta)/l \\ -x_m\ s^2\theta + \frac{y_m}{2}\ s2\theta \\ \frac{x_m}{2}\ s2\theta - y_m\ c^2\theta \\ -1 \end{bmatrix}^{\mathrm{T}} \tag{7}$$

where $D = \frac{1}{Z_1} - \frac{1}{Z_2}$, l is the length of the segment and x_m and y_m are the coordinates of its middle point.

The three visual features are defined by:

$$\mathbf{s} = \begin{pmatrix} l_y, & x_f, & \theta_r \end{pmatrix} = \begin{pmatrix} y_f - y_i, & x_f, & \theta_d - \theta_p \end{pmatrix} \tag{8}$$

where θ_d and θ_p are the orientations of projected deck alignment line and its orthogonal line belonging to the deck plane at the impact point. From (6), we directly obtain:

$$\mathbf{L}_{l_y} = \begin{bmatrix} 0 & \frac{1}{Z_i} & \frac{-y_i}{Z_i} & y_f^2 - y_i^2 & -x_f y_f + x_i y_i & -x_f + x_i \end{bmatrix} \tag{9}$$

$$\mathbf{L}_{x_f} = \begin{bmatrix} 0 & 0 & 0 & x_f\ y_f & -(1+x_f^2) & y_f \end{bmatrix} \tag{10}$$

The interaction matrix of the angle θ_r is obtained from equation (7) for the two segments respectively defined by couples of points (i,f) and (l,r), they are respectively referenced by subscripts $_d$ and $_p$:

$$\mathbf{L}_{\theta_r} = \begin{bmatrix} \frac{D_d}{l_d}\ s\theta_d - \frac{D_p}{l_p}\ s\theta_p \\ \frac{-D_d}{l_d}\ c\theta_d + \frac{D_p}{l_p}\ c\theta_p \\ \frac{-D_d(x_{d_m}\ s\theta_d - y_{d_m}\ c\theta_d)}{l_d} + \frac{D_p(x_{p_m}\ s\theta_p - y_{p_m}\ c\theta_p)}{l_p} \\ -x_{d_m}\ s^2\theta_d + \frac{y_{d_m}}{2}\ s2\theta_d + x_{p_m}\ s^2\theta_p - \frac{y_{p_m}}{2}\ s2\theta_p \\ \frac{x_{d_m}}{2}\ s2\theta_d - y_{d_m}\ c^2\theta_d - \frac{x_{p_m}}{2}\ s2\theta_p + y_{p_m}\ c^2\theta_p \\ 0 \end{bmatrix}^{\mathrm{T}} \tag{11}$$

Note that $D_d = \frac{1}{Z_i}$ since the point f is the vanishing point. For any configuration of the camera, rotation around the z-axis has no effect on the feature θ_r. For other components, some simplifications appear at the desired configuration.

B. Interaction matrix at the desired configuration

At the desired configuration, the aircraft is located along its ideal glide slope as presented in Fig. 4 and the camera is oriented as explained in Section II-B. For this desired configuration, visual features are given by $x_i = 0$, $y_i = 0$, $x_f = 0$, $\theta_d = \pi/2$, $\theta_r = 0$, $D_p = 0$, $x_{d_m} = 0$, $y_{p_m} = 0$ and $l_d = -y_f$.

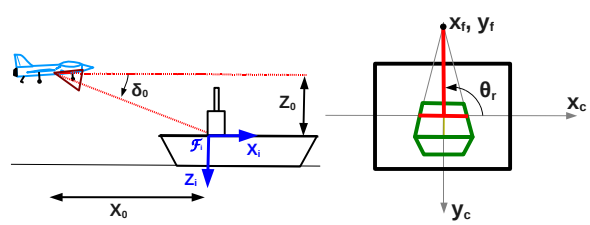

Fig. 4. Desired configuration for landing

Instantiating (9)(10) and (11), the interaction matrix $\mathbf{L_{s^*}}$ at desired configuration is given by:

$$\mathbf{L_{s^*}} = \begin{bmatrix} 0 & \frac{1}{Z_i} & 0 & y_f^2 & 0 & 0 \\ 0 & 0 & 0 & 0 & -1 & y_f \\ \frac{-1}{|y_f|\ Z_i} & 0 & 0 & 0 & 0 & 0 \end{bmatrix} \tag{12}$$

where Z_i and y_f are different of zero.

The interaction matrix $\mathbf{L_{s^*}}$ highlights why these features are interesting to land. Indeed, l_y is closely linked to longitudinal motions υ_y and ω_x whereas x_f and θ_r allow to control respectively lateral velocity υ_x and relative cap ω_y.

C. From pose to visual features

We now present the link between the aircraft pose and visual features in order to determine the relation between them at desired position. The carrier velocity is not taken into account in this modeling. Using (6), the link between aircraft velocity $\mathbf{v}_b$ and time derivative of visual features $\mathbf{s}$ is established by:

$$\dot{\mathbf{s}} = \mathbf{L_s}\ {}^c\mathbf{W}_b\ \mathbf{v}_b \tag{13}$$

where ${}^c\mathbf{W}_b$ is the velocity screw transformation matrix:

$${}^c\mathbf{W}_b = \begin{bmatrix} {}^c\mathbf{R}_b & [{}^c\mathbf{t}_b]_\times\ {}^c\mathbf{R}_b \\ \mathbf{0} & {}^c\mathbf{R}_b \end{bmatrix} \tag{14}$$

with ${}^c\mathbf{R}_b$ and ${}^c\mathbf{t}_b$ are the pose of the aircraft in the camera frame $\mathcal{F}_c$ and $[\ ]_\times$ is the skew matrix expression. For simplification purpose, ${}^c\mathbf{t}_b$ is equal to zero (we consider the camera at the cog of the aircraft).

In order to express the relation with pose derivative, (13) becomes:

$$\dot{\mathbf{s}} = \mathbf{L_s}\ {}^c\mathbf{W}_b\ {}^b\mathbf{W}_i\ \dot{\mathbf{P}} \tag{15}$$

where ${}^b\mathbf{W}_i$ is the transformation matrix obtained from (1):

$${}^b\mathbf{W}_i = \begin{bmatrix} \mathbf{B_B} & \mathbf{0} \\ \mathbf{0} & \xi^{-1} \end{bmatrix} \tag{16}$$

Instantiating (15) around the trim point defined in Section II-A, it leads to:

$$\dot{l_y} = y_f^2\ \dot{\theta} - \frac{s2\delta_0}{2\ X_0}\ \dot{X} - \frac{c^2\delta_0}{X_0}\ \dot{Z} \tag{17}$$

$$\dot{x_f} = (y_f\ c\theta_c - s\theta_c)\ \dot{\phi} - (c\delta_0 + y_f\ s\delta_0)\ \dot{\psi} \tag{18}$$

$$\dot{\theta_r} = \frac{c\delta_0}{|y_f|\ X_0}\dot{Y} \tag{19}$$

where $c\delta_0 = \cos\delta_0$ and $s\delta_0 = \sin\delta_0$.

The link between the derivative of pose and the derivative of visual features is rewritten as:

$$\dot{\mathbf{s}} = \mathbf{J_s}\ \dot{\mathbf{P}} \tag{20}$$

with, considering small angle assumption ($c\delta_0 = 1$, $s\delta_0 = 0$):

$$\mathbf{J_s} \approx \begin{bmatrix} 0 & 0 & -\frac{1}{X_0} & 0 & y_f^2 & 0 \\ 0 & 0 & 0 & y_f\ c\theta_c - s\theta_c & 0 & -1 \\ 0 & \frac{1}{|y_f|\ X_0} & 0 & 0 & 0 & 0 \end{bmatrix} \tag{21}$$

Assuming small displacement around a given pose, the integration of relation (20) leads to:

$$\tilde{\mathbf{s}} = \mathbf{J_s}\ \tilde{\mathbf{P}} \tag{22}$$

This constitutes the relation between the pose and the visual features that will be used in the control law. Visual features l_y, x_f and θ_r are respectively related to altitude, relative cap and lateral position of the aircraft with respect to the impact frame.

IV. Control law

The objective of the control is to make landing the aircraft using its internal state measured with the IMU and visual features provided by the camera.

A. System outputs

States of the aircraft, presented in equation (3) are observable using aircraft sensors and visual measurements. Thus, longitudinal and lateral outputs are composed by:

$$\mathbf{y}_{lg} = \begin{pmatrix} V, & \alpha, & \theta, & q, & l_y \end{pmatrix} \tag{23}$$

$$\mathbf{y}_{lt} = \begin{pmatrix} p, & r, & \phi, & x_f, & \theta_r \end{pmatrix} \tag{24}$$

and linked to the states by $\tilde{\mathbf{y}}_{lg} = \mathbf{C}_{lg}\ \tilde{\mathbf{x}}_{lg}$ and $\tilde{\mathbf{y}}_{lt} = \mathbf{C}_{lt}\ \tilde{\mathbf{x}}_{lt}$ where matrix $\mathbf{C}_{lg}$ and $\mathbf{C}_{lt}$ are easily obtained from (22):

$$\mathbf{C}_{lg} = \begin{bmatrix} & \mathbf{I}_{4\times4} & & & \mathbf{0}_{4\times1} \\ 0 & 0 & y_f^2 & 0 & -\frac{1}{X_0} \end{bmatrix} \tag{25}$$

$$\mathbf{C}_{lt} = \begin{bmatrix} & \mathbf{I}_{3\times3} & & \mathbf{0}_{3\times2} & \\ 0 & 0 & y_f\ c\theta_c - s\theta_c & -1 & 0 \\ 0 & 0 & 0 & 0 & \frac{1}{|y_f|\ X_0} \end{bmatrix} \tag{26}$$

$\mathbf{I}_{r\times c}$ and $\mathbf{0}_{r\times c}$ are respectively Identity and Zeros matrix, with r and c the number of rows and columns.

B. State feedback control law

As in previous works ([13][11][12][10]), state feedback is used as control law. As the state is not directly available, state is expressed using visual features contained in $\tilde{\mathbf{y}}$. Inputs are computed as follow:

$$\begin{bmatrix} \tilde{\mathbf{u}}_{lg} \\ \tilde{\mathbf{u}}_{lt} \end{bmatrix} = -\begin{bmatrix} \mathbf{K}_{lg} & \mathbf{0} \\ \mathbf{0} & \mathbf{K}_{lt} \end{bmatrix} \begin{bmatrix} \tilde{\mathbf{x}}_{lg} \\ \tilde{\mathbf{x}}_{lt} \end{bmatrix} = -\begin{bmatrix} \mathbf{K}_{lg}\mathbf{C}_{lg}^{-1} & \mathbf{0} \\ \mathbf{0} & \mathbf{K}_{lt}\mathbf{C}_{lt}^{-1} \end{bmatrix} \begin{bmatrix} \tilde{\mathbf{y}}_{lg} \\ \tilde{\mathbf{y}}_{lt} \end{bmatrix} \tag{27}$$

The system is regulated around the point $\mathbf{y}_{lg}^* = (V^*, \alpha^*, \theta^*, 0, l_y^*)$ and $\mathbf{y}_{lt}^* = (0, 0, 0, 0, -\pi/2)$. It has to be emphasized that desired state remains constant all along the descent, which is not the case with previous methods.

State feedback gains $\mathbf{K}_{lg}$ and $\mathbf{K}_{lt}$ are computed using optimal LQ method with weighting matrix defined in [16]:

$$Q = diag(1/\tilde{x}_{i_{max}}^2) \tag{28}$$

$$R = diag(1/\tilde{u}_{i_{max}}^2) \tag{29}$$

In order to simplify the control and demonstrate its robustness, matrix $\mathbf{C}_{lg}$ and $\mathbf{C}_{lt}$ are computed for a given X_0 corresponding to the mean of the longitudinal difference. Elements θ_c^* and y_f^* do not vary along the desired descent.

V. Results

This section presents results of the control law proposed in the previous section. To demonstrate the control law validity, it was tested with a simulation software provided by Dassault Aviation, which contains a realistic non-linear model of the stabilized aircraft. We consider a moving carrier at 20 kts (about 10.3 meters per second) with no attitude movement (this case will be further investigated). The wind is not considered. As usual, the deck axis of the carrier is oriented with respect to the carrier axis of an angle of about 7°. For the two simulations, desired outputs V^*, α^*, θ^* and l_y^* are respectively equal to 67 meters per second, 14 degrees, 10.3 degrees and -0.07 meters.

A. Simulated visual features

Some assumptions are led in this part whose purpose is to validate the control law. Visual features values are considered available, there is no image processing step. The aircraft is initialized near the usual position at about 7 km from the carrier. Vertical and lateral shift with respect to the ideal trajectory are respectively equal to 100 and 240 meters; moreover, a cap difference of 5 degrees is also introduced.

The alignment and landing tasks are performed with a good behavior as presented on Fig. 5, 6 and 7 which respectively present longitudinal and lateral trajectories, positioning errors between aircraft and carrier, aircraft angles and visual features. Considering a far initial position and the carrier movement, longitudinal and lateral errors (Fig. 6b) decrease smoothly with angles remaining acceptable for the aircraft. Indeed, the angle of attack, which is closely linked to the aircraft stall and stability, is varying very few, and velocity variation is inferior to 5 m/s. Moreover, lateral angles ϕ and ψ remain in the aircraft capabilities, even with a large initial position error. In the image, the time evolution of features is smooth. The small jump in the vertical trajectory at the beginning is due to the fact that, at this moment, the pitch angle is increasing (Fig. 6a). In the image (Fig. 7), the segment $[if]$ evolves far from the desired position, l_y is not invariant to pitch variation as presented in equation (12). Moreover, the lateral dynamics has an impact on l_y since we consider only the y component. Nevertheless, these couplings have not a significant effect since the landing is performed well. Considering that the carrier velocity is not taken into account, a small tracking error appears (more visible for lateral error on Fig. 6b). But this error is reduced as the distance between aircraft and carrier is reduced. Usually, tracking error remains constant at constant velocity, but using our visual features, the tracking error converges to zero at the landing (at the end of the simulation lateral error is equal to 11 cm). The lateral control is also performed without an important coupling with longitudinal control. It remains a small difference in the relative cap ψ_r of about 1°(Fig. 6a) due to the carrier velocity. In the image, it leads to a small difference for x_f and θ_r (Fig. 7) wrt the desired values.

Considering that the initial position is far from the carrier, and there is no trajectory following, the control scheme and the visual features allow to perform alignment and landing tasks with a compatibility of the aircraft dynamics.

B. Control using a 3D-model based tracker

The control law was tested with a 3D-model based tracker (presented in [1]) in a simulation environment based on a high fidelity visualization software. The sampling time of the loop is set to 50 ms. The tracker provides directly the estimated pose ${}^{c}\hat{\mathbf{M}}_d$ between the deck and the camera. In this simulation, camera used is the Damocles pod presented in Section I. Using the estimated pose, the pod tilt and roll are controlled to center the carrier in the image. Knowing the Damocles camera orientation and position ${}^{c}\mathbf{M}_b$, the pose between the aircraft and the deck ${}^{b}\mathbf{M}_d$ can be computed. We then consider a virtual static camera c_v whose orientation is

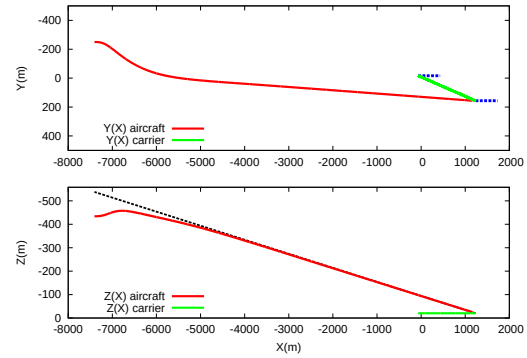

Fig. 5. Lateral and vertical trajectories of aircraft and impact point of carrier (meters); Black dash line corresponds to the glide desired; Blue dash lines are the orientation of the deck at the beginning and the end of simulation

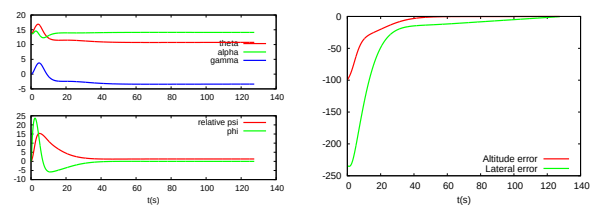

(a) (b)

Fig. 6. (a) Time evolution of angles (in degrees) for longitudinal and lateral control; (b) Time evolution of vertical and lateral errors (meters) between the aircraft and the impact point of carrier

defined as in Section II-B and positioned at the cog of the aircraft, visual features l_y, x_f and θ_r are computed using the pose ${}^{c_v}\hat{\mathbf{M}}_d$ between the deck and this virtual camera (we have ${}^{c_v}\hat{\mathbf{M}}_d = {}^{c_v}\mathbf{M}_b \; {}^{c}\mathbf{M}_b^{-1} \; {}^{c}\hat{\mathbf{M}}_d$). To summarize the method, the visual tracking is done with the swiveling Damocles camera c whereas the visual control of the aircraft is performed with a virtual fixed camera c_v.

Results using the 3D tracker are presented in Figs. 9 and 8 and in the enclosed video. To take into account the model based tracker and the camera with a FOV of 4°, the task is performed from 3500 meters from the carrier to near the touch point, and gains of the control law were reduced. In order to be representative of the operational conditions, the aircraft is initially shifted of 20 and 35 meters in vertical and lateral positions. The landing phase is performed by taking into account all the loop: dynamics, sensors, perception and control law. As in previous results, the position errors (Fig. 8c) converge to zero with a damped behavior without exceeding limitation of angles (Fig. 8b). Of course, measures of the visual features (Fig. 9c) are noisier due to the image processing step and it has to be highlighted that no filter is implemented. Moreover, it has to be emphasized that the 3D-model based tracker succeeds to track the carrier over a wide variation of the carrier size in the image (see Figs. 9a and 9b).

VI. Conclusion and Future Perspectives

This paper has presented a new set of visual features to perform automatic landing on aircraft carrier. These features

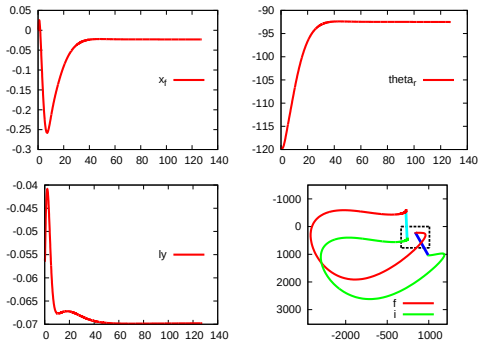

Fig. 7. Visual features simulated: Time evolution of visual features x_f, l_y (in meters) and θ_r (in degrees); Vanishing and impact point trajectories (f and i) in the image plane (in pixels)

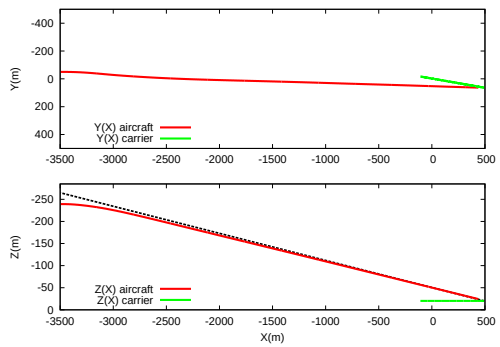

(a)

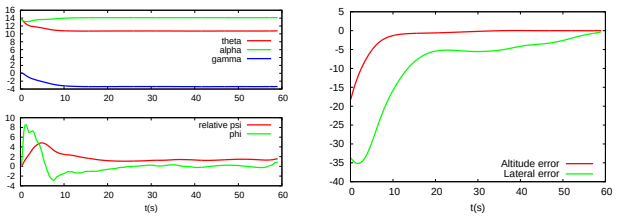

(b) (c)

Fig. 8. Control with tracker: (a) Aircraft and carrier trajectories; (b) Aircraft angles (degrees); (c) Vertical and lateral errors (meters)

were linked to the aircraft pose wrt the carrier and a control scheme was built using a linearized aircraft model. Features and control law were first tested using simulated visual features, and then on synthetic images using a 3D model based tracker. As perspectives, control schemes taking into account the wind and the carrier velocity will be investigated. Other projection models, such as spherical projection, will be also studied.

VII. Acknowledgments

This work is supported by DGA and Dassault Aviation under contribution to Laurent Coutard's Ph.D. grant. The authors would like to thank Eva Cruck from DGA and Bruno Patin from Dassault Aviation.

References

[1] L. Coutard and F. Chaumette, "Visual detection and 3d model-based tracking for landing on aircraft carrier," in *IEEE Int. Conf. on Robotics and Automation, ICRA'11*, Shanghai, China, May 2011.

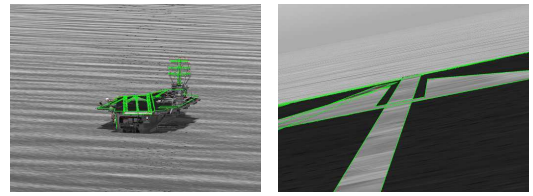

(a) (b)

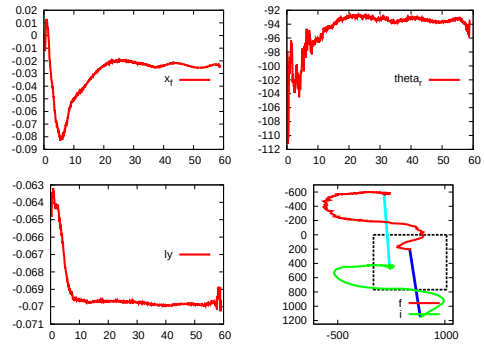

(c)

Fig. 9. First (a) and last (b) images of the simulation, green is the model projection; (c) Time evolution of visual features (in meters for x_f and l_y, in degrees for θ_r) and image trajectories of the features (pixels)

[2] P. Sousa, "Test Results of an F/A-18 Automatic Carrier Landing Using Shipboard Relative Global Positioning System," Naval Air Warfare Center Aircraft Division, Tech. Rep., 2003.

[3] B. Vu, T. Lemoing, and P. Costes, "Integration of flight and carrier landing aid systems for shipboard operations," *AGARD, Aircraft Ship Operations 15*, 1991.

[4] M. Subrahmanyam, "H infinity Design of F/A-18A Automatic Carrier Landing System," *Journal of Guidance, Control and Dynamics*, 1994.

[5] G. Galanis, A. Jennings, and P. Beckett, "Glide-Path Control Information from Runway Shape," in *SimTecT 96 Melbourne*, 1996.

[6] J. Entzinger and S. Suzuki, "Visual Cues in Manual Landing of Airplanes," in *KSAS-JSASS Joint Int. Symp. on Aerospace Engineering*, 2008.

[7] J. Naish, "Control information in visual flight," in *Seventh Annual Conference on Manual Control*, vol. 281, 1972, p. 167.

[8] P. Wewerinke, "A theoretical and experimental analysis of the outside world perception process," in *NASA. Ames Res. Center The 14 th Ann. Conf. on Manual Control*, 1978, pp. p 535–555.

[9] F. Chaumette and S. Hutchinson, "Visual servo control, part i: Basic approaches," *IEEE Robotics and Automation Magazine*, vol. 13, no. 4, pp. 82–90, December 2006.

[10] P. Rives and J. Azinheira, "Linear structures following by an airship using vanishing point and horizon line in a visual servoing scheme," in *IEEE Int. Conf. on Robotics and Automation, ICRA'04*, 2004.

[11] O. Bourquardez and F. Chaumette, "Visual servoing of an airplane for alignment with respect to a runway," in *IEEE Int. Conf. on Robotics and Automation, ICRA'07*, Rome, Italy, 2007, pp. 1330–1335.

[12] T. Gonçalves, J. Azinheira, and P. Rives, "Homography-based visual servoing of an aircraft for automatic approach and landing," in *IEEE Int. Conf. on Robotics and Automation, ICRA'10*, 2010, pp. 9–14.

[13] O. Bourquardez and F. Chaumette, "Visual servoing of an airplane for auto-landing," in *IEEE/RSJ Int. Conf. on Intelligent Robots and Systems, IROS'07*, San Diego, CA, 2007, pp. 1314–1319.

[14] J. Azinheira and P. Rives, "Image-Based Visual Servoing for Vanishing Features and Ground Lines Tracking: Application to a UAV Automatic Landing," *Int. Journal of Optomechatronics*, vol. 2, no. 3, 2008.

[15] F. Le Bras and T. Hamel, "Nonlinear Image-Based Visual Servo Controller for Automatic Landing Guidance of a Fixed-Wing Aircraft," in *European Control Conference, ECC'09*, 2009.

[16] B. Stevens and F. Lewis, *Aircraft control and simulation*. Wiley, 1992.